Time domain compressive beam forming of ultrasound signals

Guillaume David, Jean-luc Robert, Bo Zhang, and Andrew F. Laine

Citation: The Journal of the Acoustical Society of America **137**, 2773 (2015); doi: 10.1121/1.4919302
View online: https://doi.org/10.1121/1.4919302
View Table of Contents: http://asa.scitation.org/toc/jas/137/5
Published by the Acoustical Society of America

Time domain compressive beam forming of ultrasound signals

Guillaume David[a)]
Heffner Biomedical Imaging Laboratory, Biomedical Engineering Department, Columbia University, 351 Engineering Terrace MC-8904, 1210 Amsterdam Avenue, New York, New York 10027, USA

Jean-luc Robert
Philips Research North America, 345 Scarborough Road, Briarcliff Manor, New York 10510, USA

Bo Zhang
Medisys, Philips Research France, 33 rue de Verdun, 92156 Suresnes, France

Andrew F. Laine
Heffner Biomedical Imaging Laboratory, Biomedical Engineering Department, Columbia University, 351 Engineering Terrace MC-8904, 1210 Amsterdam Avenue, New York, New York 10027, USA

(Received 20 December 2014; revised 4 March 2015; accepted 30 March 2015)

Ultrasound imaging is a wide spread technique used in medical imaging as well as in non-destructive testing. The technique offers many advantages such as real-time imaging, good resolution, prompt acquisition, ease of use, and low cost compared to other techniques such as x-ray imaging. However, the maximum frame rate achievable is limited as several beams must be emitted to compute a single image. For each emitted beam, one must wait for the wave to propagate back and forth, thus imposing a limit to the frame rate. Several attempts have been made to use less beams while maintaining image quality. Although efficiently increasing the frame rate, these techniques still use several transmit beams. Compressive Sensing (CS), a universal data completion scheme based on convex optimization, has been successfully applied to a number of imaging modalities over the past few years. Using *a priori* knowledge of the signal, it can compute an image using less data allowing for shorter acquisition times. In this paper, it is shown that a valid CS framework can be derived from ultrasound propagation theory, and that this framework can be used to compute images of scatterers using only one plane wave as a transmit beam.
 [http://dx.doi.org/10.1121/1.4919302]

[KGS] Pages: 2773–2784

I. INTRODUCTION

Over the past decade, Compressive Sensing (CS) has gained a lot of visibility and recognition from the signal processing community. This inverse problem technique allows for drastic down-sampling of a signal and relies on computational power as well as *a priori* information, in the form of the knowledge of a basis where the signal has a *sparse* representation, to account for the missing samples, and uses convex optimization to reconstruct the signal.

The seminal work of Candès,[1] Baraniuk,[2] Romberg,[3] etc., has led to innovations in a lot of different fields ranging from astronomy to seismology and radars. This technology is currently used in some commercial magnetic resonance imaging (MRI) scanners. In MRI, the gain for a higher acquisition rate is obvious: by allowing a smaller number of measurements, it enables shorter acquisition times,[4] resulting in less discomfort for the patient, less artifacts, and a higher daily patient turnover. For echography, the applications could go from fast three-dimensional (3D) echocardiography to simplified echography systems for example.

Classic beam forming schemes use many transmit waves to insonify a medium,[5] and sample echoes at a high acquisition rate of tens of millions of samples per second. While many successful attempts to reduce the number of transmit waves have been made, several beams are still necessary to maintain good image quality.[6,7] One of the advantages of CS is its ability to require less information for accurate reconstruction when certain mathematical conditions hold. As far as ultrasound imaging is concerned, two aspects of beam forming or image formation could benefit from this new approach. In medical echography, the reconstruction of an image classically requires expensive arrays made of hundreds of transducers that emit sequences of focalized transmit pulses.[5] First, CS could mean implementing simplified hardware such as an ultrasonic probe with a small number of independent transducers, making ultrasonic systems more affordable. Then, it could mean using less transmit pulses, making the acquisition faster and the frame rate higher.

CS has started to receive the attention of acoustics physicists. It has been successfully implemented in the frequency domain by Schiffner and Schmitz,[8] it has been used with wave atoms and wavelets by Friboulet *et al.*,[9] and in the *Xampling* framework by Eldar *et al.*[10] Our approach is different in the sense that it is a time domain implementation of CS, and aims at reducing both the number of transmit waves and the number of receiving transducers, while decreasing the sampling frequency. To the best of our knowledge, it is the first article that justifies formally the CS framework in

[a)]Electronic mail: gd2346@columbia.edu

the time domain. This work can be put into the perspective of Ref. 8 as the time and frequency domains are related to each other by the Fourier transform.

This article focuses on the beam forming of ultrasonic fields and introduces the CS approach in a medium containing only a few point scatterers. First, a brief overview of CS is given, along with a simple example. Then, the approach is justified using the theory of wave propagation in a homogeneous medium, and the fundamentals of the theory are laid out. In addition, simulation results are presented alongside the limitations of the described approach. Further developments to overcome these limitations are proposed. Finally, images of a phantom are shown and compared against a state-of-the-art reconstruction algorithm.

II. BEAM FORMING IN A HOMOGENEOUS MEDIUM

A. Focusing in transmission

Focusing in a homogeneous medium is currently achieved on most commercial scanners by using ultrasonic probes made of an array of independent transducers. Each transducer is connected to a separate delay line as presented in Fig. 1. They are commonly referred to as "channels." The size of the elements of the array and the spacing between them are about the size of the central wavelength of the probe or smaller. Under those conditions, the side lobes remain small and the grating lobes are minimized,[11] ensuring proper focalization of the energy in the medium. Each element emits the same pulse but at different times. The propagation time or time-of-flight (ToF) between each element and the focal point are calculated. From those values, delays are inferred and applied in emission so that the pulses emitted by each individual element reach the target focal point at the same time, thus interfering constructively at that location. To obtain a sharp image with the least amount of noise, a sequence of focalized pulses is emitted in different directions, and the acquired echoes are combined off-line to form an image. That last step relies on *in silico* focalization easily made possible by a direct access to the phase of the sound waves.

B. Beam forming in reception

Beam forming in reception or image formation is a similar process. The final image is an echo intensity map that shows the acoustic echogenicity of the medium. The greater the echogenicity, the more intense the echo. The intensity is

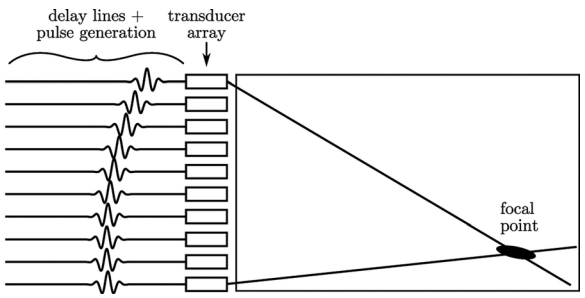

FIG. 1. Beam steering in transmission: delays are calculated so that the waves emitted by each independent element reach the target focal point at the same time, interfering constructively.

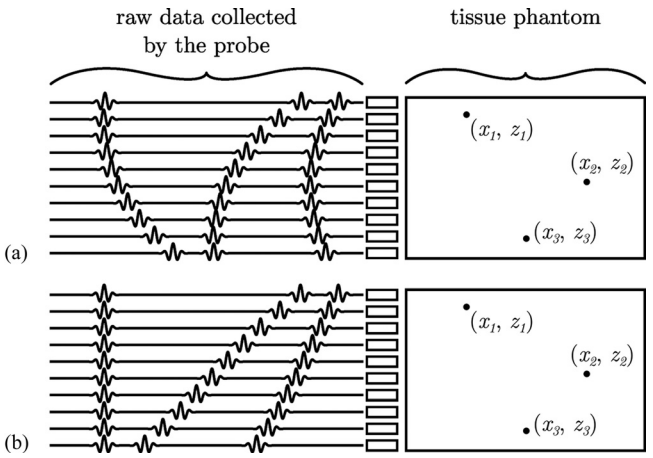

FIG. 2. Beam forming in reception: (a) the echoes coming from three point scatterers are acquired by the probe; (b) ToFs from (x_1, z_1) to each transducer are calculated and applied to the channels, aligning the phase of the wavefronts coming from that point.

computed using off-line focusing. The intensity of the sound reflected in a particular point (x_i, z_i) of the medium being imaged is obtained by computing the ToF from each element of the ultrasonic probe to the point (x_i, z_i) and back. From those values, delays are inferred and applied in reception so that all the echoes originating from (x_i, z_i) are propagated back to that point. As shown in Fig. 2, applying the calculated delays to each channel aligns the waveforms originating from (x_i, z_i), whereas the echoes originating from other locations do not get aligned. Finally, the channels are summed together, and the waves originating from (x_i, z_i) interfere constructively, the delays applied to each channel making them perfectly in phase. The waves originating from other locations get averaged out to small values as they are not in phase. It is the principle of coherent summation. This process is repeated for all the points (x_i, z_i) of the final image, and the amplitude value for each point is stored in the corresponding pixel. This algorithm is known as Delay-and-Sum (DAS).[12] It is worth noting that to the best of the authors knowledge it has not been proven that DAS is the best way to solve this inverse problem, leaving a lot of potential for new algorithms and innovations.

III. OVERVIEW OF CS

Over the past 10 years, CS has gained a lot of visibility from the medical imaging research community. The most compelling feature for the use of CS is its ability to perform perfect reconstructions of under-sampled signals using l_1-minimization. Of course, that counter-intuitive feature does not come without a cost. The lacking information is compensated for by *a priori* knowledge of the signal, as well as certain conditions detailed further in the article.

So far, CS has proven to be particularly well suited for MRI, where the assumptions of the CS theory can easily be justified, and the implementation is fairly straightforward.[4] It has allowed for faster image acquisition without loss in image quality and resolution, which is critical for applications such as cardiac MRI. The application of CS to ultrasound imaging

is not as straightforward due to the very nature of the acquired signal and the inverse problem that needs to be solved.

This section presents the basics of CS and aims at giving the reader the minimal background necessary to understand the assumptions and underlying constraints of this technique.

A. Fundamentals of CS

CS relies mainly on two fundamental assumptions related to the acquired signal: *sparsity* and *coherence*. The sparsity assumption is used in the form of an l_1-norm minimization, a natural promoter of sparsity. The energy of a sparse signal in a certain basis is concentrated on a few samples. The target number of acquisition being low, each measurement has to provide as much information as possible. For that reason the acquisition is performed on a different basis where the energy of the signal is spread out on as many samples as possible. Intuitively, the two bases are incoherent, enabling fewer measurements containing all the information required for accurate reconstruction.

1. Sparsity

A vector $I \in \mathbb{R}^N$ is said to be S-sparse if all but S of its coefficients are equal to zero. Considering a basis $(\varphi_k)_{k=1,\dots,N}$ of the signal space, the vector I is written

$$I = \sum_{k=1}^{N} I_k \varphi_k, \tag{1}$$

where $(I_k)_{k\in(1,\dots,N)}$ are its coefficients in the basis (φ_k). In that framework, I is said to be S-sparse if the subset $\Omega = \{k \,|\, I_k \neq 0\}$ is of cardinality S. Equivalently the condition $\|I\|_{l_0} \leq S$ must hold true. $\|I\|_{l_0}$ is the l_0-pseudonorm defined as the number of non-zero coefficients of I.

2. Incoherence

The coherence between two bases Φ and Ψ of a given space is usually defined as the maximum absolute value of the cross-correlation between the elements of the two bases[13]

$$\mu(\Phi, \Psi) = \sqrt{N} \cdot \max_{1\leq k,j\leq N} |\langle \varphi_k, \psi_j \rangle|. \tag{2}$$

In CS, we are looking at low μ values which corresponds to *incoherent* bases.

3. Description of the framework

Let us consider a signal f. We assume that f has a sparse representation I in the basis ψ, represented by the matrix Ψ. Thus we have $f = \Psi I$. The acquisition performed in the basis φ represented by the matrix Φ results in the data vector $R_0 = \Phi f$. For example, in the case of MRI, φ could be a Fourier basis. The coherence between Φ and Ψ is assumed to be low.

CS focuses on under-sampled signals. Thus, if R_0 is a vector sampled at the Nyquist frequency and has N samples, we only consider a subset Ω_u of samples with cardinality $M \leq N$. The under-sampling or decimation is modeled by the matrix denoted $D \in \mathcal{M}_{M,N}(\mathbb{R})$. The under-sampled data may then be written $R = D\,\Phi f$. Subsequently, we have $R = GI$ with $G = D\,\Phi\,\Psi$; so there exists a linear application that links the sparse representation of the signal, I, and the acquired data, R.

Under the assumptions that the signal is sparse in some basis ψ and that the bases ψ and φ are incoherent, the theory of CS states that the original signal f can be reconstructed from the under-sampled subset of coefficients R using l_1-minimization.[1] That is, the problem

$$\min_{\hat{I}\in\mathbb{R}^N} \|\hat{I}\|_{l_1} \text{ subject to } G\hat{I} = R, \tag{3}$$

where $\|I\|_{l_1} = \sum_i |I_i|$, has a unique solution $\hat{I}_0$. It can be proved that the solution is actually $\hat{I}_0 = I$. This result can then be used to recover $f = \Phi\hat{I}_0 = \Phi I$.

Equation (3) simply states that we aim at iteratively minimizing the l_1-norm of a vector $\hat{I}$ under the constraint $G\hat{I} = R$. That constraint ensures that $\hat{I}$ stays consistent with the acquired data throughout the minimization process. This problem is known as the Basis Pursuit (BP).[14]

In the presence of noise, the constraint may be relaxed and the problem becomes

$$\min_{\hat{I}\in\mathbb{R}^N} \|\hat{I}\|_{l_1} \text{ subject to } \|G\hat{I} - R\|_{l_2} \leq \varepsilon, \tag{4}$$

where ε is the noise level. This minimization problem is known as Basis Pursuit De-Noising (BPDN).[14]

As a last remark, we will note that the signal does not have to be exactly sparse in some bases. In fact, it is almost never the case with physical signals. Compressibility is sufficient: a signal f is compressible in the basis Ψ if its coefficients ordered by magnitude decay relatively fast. In that perspective, CS is a more efficient way to acquire the same amount of information from a signal.

For more information on the theory of CS, the interested reader could refer to Refs. 1–3, 13, 15, and 16.

B. 1D example: Focal plane of an ultrasound probe

As a first, simple one-dimensional (1D) example, we consider an ultrasonic transducer emitting monochromatic waves and its focal plane. The resolution in the focal plane is limited by the wavelength λ, so the focal plane of the transducer is spatially sampled in azimuth at $\lambda/2$ and for each point a corresponding plane wave is generated. This assumption corresponds to the Fraunhofer[17] approximation. In that case, the two bases are linked by the Fourier transform.

The diffraction theory states that in the focal plane, perpendicular to the probe, the amplitude of the focal point is described by a sinc function. In the conditions of the experiment, the main lobe has a width of λ and the zeros of the sinc are located every $\lambda/2$. Therefore, a spatial sampling of the focal plane at $\lambda/2$ is enough to acquire all the information needed according to Shannon-Nyquist theorem of sampling. When the main lobe of a sinc is centered on a spatial sample, the image vector is a Dirac δ function, as all the

samples except for the main lobe are located on zeros of the sinc function. As a result, the focal plane is described mathematically by the set of functions

$$\varphi_j = \delta\left(x - j\frac{\lambda}{2}\right), \tag{5}$$

where δ is the Dirac delta function and j is an integer. The plane wave basis may be written

$$\psi_l = e^{i\mathbf{k_l}\cdot\mathbf{r}}, \tag{6}$$

where $\mathbf{k_l}$ is a propagation vector, $\mathbf{r}$ is a position vector, and l is an integer. The latter expression may be simplified as the field is observed on the surface of the probe, at $z = 0$. For the sake of simplicity, the projection of the propagation vector onto the x axis is denoted k_l, and the basis becomes

$$\psi_l = e^{ik_l x}. \tag{7}$$

A diagram of the bases is shown in Fig. 3. The signification of those two bases is straightforward: a point scatterer in the image is represented by a Dirac δ function. The plane wave corresponds to the wave emitted when the scatterer is insonified, which means that for each and every scatterer in the focal plane, we associate a plane wave propagating from the scatterer to the probe. It is common knowledge that when the Nyquist criterion holds, the two bases are orthonormal and linked by the Fourier transform.

The term "image" refers here to a 1D representation of the focal plane of the probe in azimuth.

C. Results

Using this framework, we realize the following *in silico* experiment. We simulate a generic, 4 MHz central frequency probe with the following parameters: $\lambda = 385\ \mu$m, $N_{\text{elements}} = 128$, inter-element pitch $p = \lambda/2$, and $c_{\text{sound}} = 1540\ \text{m s}^{-1}$. The focal plane is located at a 7 cm depth. In the experiment, we realize the measurements using a subset of only 32 central transducers. The goal of the simulation is to show that CS preserves resolution even when a smaller number of transducers is used in reception.

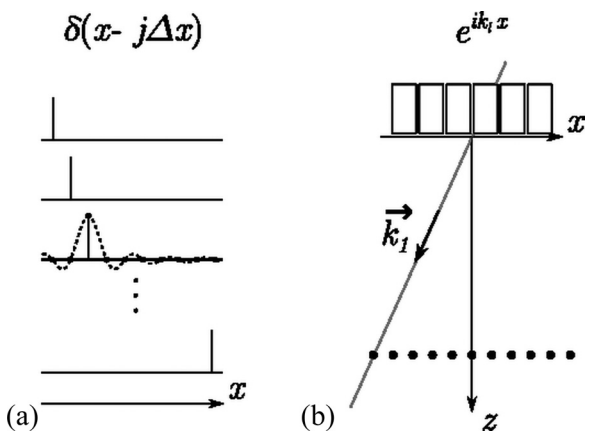

FIG. 3. (a) Basis of the focal plane of the probe, here a Dirac δ function basis with $\Delta x = \lambda/2$; the continuous intensity distribution at the focal point is also given. (b) Plane wave basis, the first $\mathbf{k_l}$ is represented. The transducers are represented by the rectangles along the x axis.

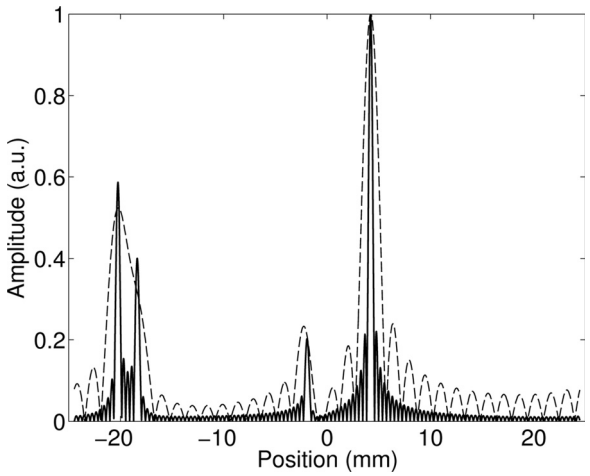

FIG. 4. 1D projection of the focal plane with 4 scatterers using only 32 of the central transducers of the probe. The signal is interpolated in the Fourier domain to show the difference in resolution: the dashed line corresponds to the image without CS, the continuous line shows the image with CS. The two scatterers on the far left are separated only when CS is used.

We simulate four scatterers in the focal plane, with different amplitudes. Those amplitudes are stored in a vector u. The matrix Φ is simply the identity matrix, and the columns of the matrix Ψ are $e^{ik_l x}$. The under-sampling matrix D restricts the acquisition to the 32 central transducers of the probe, for example. This way, we have

$$R = D\,\Phi\Psi I = GI, \tag{8}$$

where R is the data vector as acquired by our system and I is a map of scatterers in the focal plane. The minimization is performed using SPGL1.[18]

A reference image vector was computed using the Fourier transform of the under-sampled raw data R as the Fourier transform is indeed the direct relationship that links ψ and φ. Figure 4 shows a comparison in terms of resolution between the image one would obtain with the 32 central transducers, with and without CS. Unsurprisingly, the direct image exhibits the resolution of a narrower 32 transducer probe. Nevertheless, CS was able to perform the reconstruction with the resolution of the wider 128 transducer probe.

This simple simulation suggests that CS could be used in the field of ultrasonic imaging and would contribute toward simpler hardware, for example. A simpler probe with less transducers could reduce costs while CS would preserve the resolution of the final image.

IV. TIME DOMAIN 2D COMPRESSED BEAM FORMING

In the field of medical ultrasound imaging, it is more common to work on two-dimensional (2D) or 3D images than 1D representations. In this section, we introduce a CS approach to the 2D image formation paradigm. The approach, based on the use of simulated Green's functions, is justified in the following way: first, we prove that beam forming can be put in the form of a matrix multiplication.

Indeed, the CS framework requires that the acquisition vector or the *raw data* R and the image I, assuming that it is sparse, be linked by a linear operator G such that $R = GI$. Then we explain how time-domain Compressed Beam forming (t-CBF) may be performed using G as a waveform dictionary on which the sparse representation of the image is projected. Finally, we show the equivalence between this matrix multiplication form and the classic DAS algorithm.

A. 2D beam forming matrix

1. Linear beam forming operator G

One of the burning issues of CS is to find a suitable matrix G that follows the mathematical conditions of CS. It must link a sparse representation of our image, and the data in the acquisition space. Let us consider a homogeneous medium with a distribution of scatterers of reflectivity $I(\mathbf{r})$, where $\mathbf{r} = \binom{x}{z}$, denotes a position vector. An array of transducers is used for the acquisition. The array emits a sound wave that propagates through the medium to the scatterers. The scatterers reflect the excitation wave and these echoes, propagating back to the array, are acquired by the transducers. The acquisition is thus bi-dimensional, as each sample corresponds to a particular instant in time and a particular position in space. We consider each spatio-temporal sample acquired after insonification of the medium by a single wave as a measurement, in the CS terminology. Classic beam forming schemes use many transmit waves to insonify the medium, and sample the echoes at a high rate of several million samples per second. Thus, some strategies can be envisioned and combined to compress the acquisition: first the acquisition of a single image could be done with less transmit waves, then the hardware could be simplified to use less independent transducers. Finally, a lower sampling frequency could reduce the amount of data transferred to the scanner. In the following development, we focus on a single plane wave excitation of the medium. However, the formalism hence introduced can be easily generalized to any kind of excitation wave.

Let $R \in \mathcal{M}_{N_t,N_{\text{el}}}(\mathbb{R})$ be a matrix containing the raw data after only one insonification. N_t is the number of time samples, N_{el} is the number of transducers used during the acquisition. $I \in \mathcal{M}_{N_x,N_z}(\mathbb{R})$ is the original distribution of scatterers, and it corresponds to our final image. N_x and N_z are the number of pixels in azimuth and depth, respectively. To apply the principles of CS, we need to define a linear relationship between the data R and the image I. Namely we are looking for a tensor $G \in \mathcal{M}_{N_t,N_{\text{el}},N_x,N_z}(\mathbb{R})$ such that

$$R = GI. \tag{9}$$

In order to define the matrix G, the acquisition process is broken down into the following steps. First, the transducers of the array are excited by an electrical temporal impulse denoted by $h^i_{\text{ex}}(t)$ for the ith transducer. The transducers are considered to have equivalent physical properties, and have the same impulse response denoted by $h_{\text{trans}}(t)$. As a result, the impulse response of the acquisition system in emission is

$$h^i_{\text{sys,Tx}}(t) = (h^i_{\text{ex}} \underset{t}{\otimes} h_{\text{trans}})(t). \tag{10}$$

Expression (10) takes into account the impulse response of the acquisition system in emission which includes the central frequency and bandwidth of the probe as well as the transmitted amplitude.

The sound wave thus emitted propagates through the medium from the array to each scatterer. The impulse response of the forward propagation process of the emitted wave is denoted by $h_{\text{fwd}}(t_c, \mathbf{r})$. Part of the energy of the wave gets reflected by the scatterers in the form of spherical waves. The reflected amplitude for each scatterer is given by the reflectivity $I(\mathbf{r})$. The impulse response of the backward propagation process is denoted by $h^i_{\text{bwd}}(t_c, \mathbf{r})$, the index i corresponding to the index of the transducer used for the acquisition. Finally, the pressure field is converted into an electrical signal by the probe and acquired by the scanner, with the impulse response $h_{\text{trans}}(t)$ mentioned earlier.

We can now infer the mathematical expression of the total pressure field recorded by the probe by convolving in time the different terms aforementioned and summing over space

$$R^i(t) = \int_{\mathbf{r}} \left(h^i_{\text{sys,Tx}}(t_c) \underset{t_c}{\otimes} h_{\text{fwd}}(t_c, \mathbf{r}) \underset{t_c}{\otimes} h^i_{\text{bwd}}(t_c, \mathbf{r}) \underset{t_c}{\otimes} h_{\text{trans}}(t_c) \right)(t) \cdot I(\mathbf{r}) d\mathbf{r}, \tag{11}$$

under the assumption that multiple scattering is negligible which is a classic approximation in medical ultrasound imaging.

In Eq. (11), the terms $h^i_{\text{sys,Tx}}$ and h_{trans} can be grouped: they describe the impulse response of the acquisition system, denoted $h^i_{\text{sys, TxRx}}$. $h^i_{\text{sys, TxRx}}$ takes into account the central frequency of the probe, as well as its bandwidth, usually modeled by a Gaussian function. As a result, for the sake of simplicity we can leave that term out of the development, keeping in mind that depending on the parameters of the probe, those terms have to be added back when calculating the matrix G. This leads to

$$R^i(t) = \int_{\mathbf{r}} \left(h_{\text{fwd}}(t_c, \mathbf{r}) \underset{t_c}{\otimes} h^i_{\text{bwd}}(t_c, \mathbf{r}) \right)(t) \cdot I(\mathbf{r}) d\mathbf{r}. \tag{12}$$

The next step is to discretize the simplified Eq. (12). The time variable t becomes $t_j = j\Delta t$ where $\Delta t = 1/f_s$, f_s being the sampling frequency of the system. The spatial variable $\mathbf{r}$ becomes $\mathbf{r_{kl}} = \binom{x_k}{z_l} = \binom{k\Delta x}{l\Delta z}$, where Δx and Δz are the grid spacing in azimuth and depth, respectively. This yields

$$R_{ij} = \sum_{k=1}^{N_x} \sum_{l=1}^{N_z} \cdot \left(h_{\text{fwd}}(t_c; k, l) \underset{t_c}{\otimes} h^i_{\text{bwd}}(t_c; k, l) \right)(j) I_{kl}. \tag{13}$$

Equation (13) is indeed a tensor product between a bi-dimensional matrix $I = (I_{kl})_{k,l}$ and a four-dimensional tensor $G = (G_{ijkl})_{i,j,k,l}$. Following this notation, we have

$$G_{ijkl} = \left(h_{\text{fwd}}(t_c; k, l) \underset{t_c}{\otimes} h^i_{\text{bwd}}(t_c; k, l) \right)(j), \tag{14}$$

that may be discretized to

$$G_{ijkl} = \sum_{u=1}^{N_t} h_{\text{fwd}}(j-u;k,l)h^i_{\text{bwd}}(u;k,l). \tag{15}$$

Based on this framework, we can particularize the solution. For a plane wave excitation propagating along the axis of the probe in a homogeneous medium [Fig. 5(a)], the propagation to a scatterer in $\mathbf{r} = \binom{x}{z}$ can be modeled by the following forward impulse response:

$$h^i_{\text{fwd}}(t,\mathbf{r}) = \delta\left(t - \frac{z}{c}\right), \tag{16}$$

which does not depend on the emitting transducer i in the case of a plane wave excitation: the individual excitation pulses are synchronized on all the channels.

After propagation through the medium, the plane wave reaches a scatterer in $\mathbf{r}$ and gets reflected. The scatterer is assumed to be smaller than λ, thus generating a spherical wave which yields to the following backward impulse response that describes the propagation from the scatterer in $\mathbf{r}$ back to the ith transducer of the array[19]

$$h^i_{\text{bwd}}(t,\mathbf{r}) = \frac{\delta\left(t - \frac{\|\mathbf{r}-\mathbf{r_i}\|}{c}\right)}{2\pi\|\mathbf{r}-\mathbf{r_i}\|}, \tag{17}$$

which is the Green's function of the homogeneous medium [Fig. 5(b)].

From Eqs. (16) and (17), we can infer the mathematical expression of the pressure field resulting from an excitation of the medium by a plane wave and its reflection on a scatterer located in $\mathbf{r}$,

$$h_{\text{fwd}}(t_c,\mathbf{r}) \underset{t_c}{\otimes} h^i_{\text{bwd}}(t_c,\mathbf{r})(t) = \frac{\delta\left(t - \frac{z}{c} - \frac{\|\mathbf{r}-\mathbf{r_i}\|}{c}\right)}{2\pi\|\mathbf{r}-\mathbf{r_i}\|}. \tag{18}$$

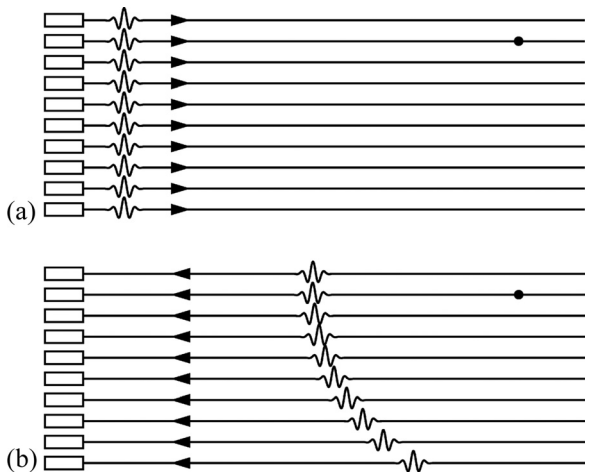

FIG. 5. (a) The pressure field in the medium after emission by the ultrasonic probe. The black dot is a scatterer. The arrow indicates the direction of propagation of the ultrasonic wave. (b) The pressure field after reflection on the scatterer.

Discretizing Eq. (18) leads to the following expression for G_{ijkl}:

$$G_{ijkl} = \frac{\delta\left(t_j - \frac{z_l}{c} - \frac{\|\mathbf{r_{kl}}-\mathbf{r_i}\|}{c}\right)}{2\pi\|\mathbf{r_{kl}}-\mathbf{r_i}\|}. \tag{19}$$

Equation (19) corresponds to the diffraction impulse response of a homogeneous medium with one point scatterer located at $\mathbf{r_{kl}}$; in other words the Green's function of the medium that takes into account both the transmission and the reception parts. Therefore, G_{ijkl} is the Green's function of the medium, observed at the time sample j by the ith transducer when a point scatterer is at the position $\mathbf{r_{kl}}$ in space.

We have defined a four-dimensional tensor G that gives a linear relationship between a map of scatterers I in a homogeneous medium, and the raw data R acquired by the array of transducers:

$$R = GI. \tag{20}$$

For CS, we need to write Eq. (20) in the form of a matrix product. To that end, we perform a change of indexes going from (i,j,k,l) to (α,β) with

$$\begin{cases} \alpha = j + N_t(i-1) \\ \beta = l + N_z(k-1), \end{cases} \tag{21}$$

which is a bijective $\mathcal{C}^1$ change of variable.

With that notation, we have

$$R_\alpha = G_{\alpha\beta}I_\beta \tag{22}$$

using Einstein's convention, where the repeated index β is implicitly summed across all its accessible values.

2. Relationship with DAS

The standard beam forming algorithm described in the literature and widely used in available commercial scanners, called the DAS, is a reconstruction algorithm that computes an image D based on the raw data R by using the principle of coherent summation.[12] In that framework, the propagation delays from the surface of the transducers to the different points of the final image defined by the grid $\mathcal{G}$ are applied to each channel of the raw data before summation and detection. Thus, the level value of the pixel (k,l) in the image D is given by

$$D_{kl} = \sum_{i=1}^{N_{\text{el}}} R\left(\mathbf{r_i}, \frac{z_l}{c} + \frac{\|\mathbf{r_{kl}}-\mathbf{r_i}\|}{c}\right), \tag{23}$$

where the term $(z_l/c) + (\|\mathbf{r_{kl}}-\mathbf{r_i}\|/c)$ corresponds to the propagation time, back and forth, from the probe's ith element to the position $\mathbf{r_{kl}}$ for a plane wave excitation.

The right-hand side of Eq. (23) can be interpreted as a convolution product of $R(\mathbf{r_i},t)$ and $\delta(t-(z_l/c)+(\|\mathbf{r_{kl}}-\mathbf{r_i}\|/c))$. In discrete time, we have

$$D_{kl} = \sum_{i=1}^{N_{el}} \sum_{j=1}^{N_t} \delta\left(t_j - \frac{z_l}{c} - \frac{\|\mathbf{r_{kl}} - \mathbf{r_i}\|}{c}\right) \cdot R(\mathbf{r_i}, t_j). \quad (24)$$

DAS classically neglects the amplitude term $(1/2\pi\|\mathbf{r_{kl}} - \mathbf{r_i}\|)$ that is due to propagation[12] as well as the impulse response of the transducer. The interested reader can refer to Ref. 20 that describes a back propagation beam forming algorithm that does not neglect the amplitude term and the impulse response of the transducer, and Ref. 21 that describes a matched filter approach to beam forming that also accounts for the amplitude term by modeling the wavefront propagation. Adding that term back in Eq. (24), we find that DAS is equivalent to

$$D = G^{\mathsf{T}} R, \quad (25)$$

which involves the same matrix G as we are using in the t-CBF framework. Subsequently, G can be interpreted as a beam forming matrix. The final image D is obtained by successive projections of the raw data on the columns of dictionary G.

Equations (20) and (25) together define a direct relationship between the DAS image D and the scatterer distribution I:

$$D = G^{\mathsf{T}} G I. \quad (26)$$

From this, we can sense the importance of the matrix $G^{\mathsf{T}}G$: it links the scatterer distribution to the final DAS image and can therefore be seen as a Point Spread Function (PSF) of the acquisition system. As we will see further in the development the *mutual coherence* of that matrix, that accounts for the similarity of its column vectors, is of tremendous importance in the resolution achievable in both DAS and t-CBF frameworks.

Equation (26) also shows that we should expect the DAS and the t-CBF images to be different in nature.

3. Practical implementation

In the previous development, we established a formal expression for G_{ijkl} leaving out the influence of the parameters of the acquisition system such as the central frequency f_c, and the bandwidth bw of the probe. The bandwidth is generally modeled by a Gaussian function. Usually, the electrical excitation pulse h^i_{ex} is a simple temporal Dirac δ pulse. In the case of a plane wave, the pulses are synchronized on all the channels, therefore $h^i_{\text{sys, Tx}}$ does not depend on i and is equal to h_{trans}. Finally, the term $h^i_{\text{sys, TxRx}}$ from Eq. (11) is the auto-convolution of the Gaussian pulse, which can be approximated by another Gaussian pulse of same central frequency f_c and bandwidth $(\sqrt{2}/2)bw$,

$$h_{\text{sys, TxRx}}(t) \approx \text{gauspuls}\left(t, f_c, \frac{\sqrt{2}}{2} bw\right), \quad (27)$$

where the function gauspuls is defined by

$$\text{gauspuls}(t, f_c, bw) = e^{-(t^2/2t_v)} \cos(2\pi f_c t) \quad (28)$$

with $t_v = -[8 \log(10^{-6/20})/4\pi^2 bw^2 f_c^2]$.

To get the final expression for G_{ijkl}, expression (19) is convolved with $h_{\text{sys, TxRx}}$,

$$G_{ijkl} = \text{gauspuls}\left(t_j - \frac{z_l}{c} - \frac{\|\mathbf{r_{kl}} - \mathbf{r_i}\|}{c}, f_c, \frac{\sqrt{2}}{2} bw\right), \quad (29)$$

which is the expression used in Sec. V.

Therefore, in this particular setting, we can link a point scatterer at a certain location with a wavefront recorded by the probe, or simulated, as shown in Fig. 6. By repeating this process for all the points of a grid $\mathcal{G}$ that spans the whole final image space, one can populate a dictionary of wavefronts G that links a map of scatterers in a medium to the pressure field generated by them and acquired by the probe. Intuitively, one can expect this dictionary to be suitable for CS as long as the number of scatterers in the medium is small enough to ensure sparsity, and the grid spacing in depth and azimuth is chosen wisely, to ensure that the dictionary has a low coherence.

B. Toward a compressed beam forming algorithm

According to the definition of G, each of its columns contains the Green's function of a given scatterer. In that sense, it is a dictionary of Green's functions that associates a diffraction impulse response to a distribution of scatterers.

So within the limitations of our model, if R is a signal acquired with the ultrasonic probe, then there exists a spatial distribution of scatterers I such that

$$R = GI. \quad (30)$$

Using Eq. (30), we may infer a BP beam forming algorithm based on l_1-minimization

$$\min_{\hat{I} \in \mathbb{R}^{\mathbb{N}_{\text{img}}}} \|\hat{I}\|_{l_1} \text{ such that } R = G\hat{I} \quad (31)$$

in the absence of noise and if the distribution of scatterers I is *sparse*.

In order to take into account the acquisition noise, and the inaccuracies of our model, one can relax the constraint with an inequality:

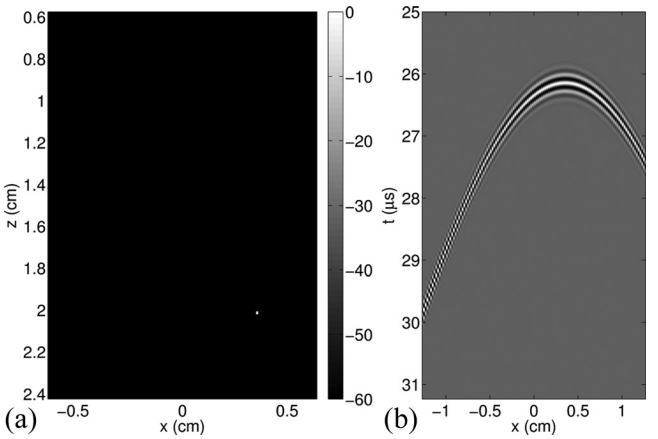

FIG. 6. Representation of a point scatterer in (a) the image space and (b) the acquisition space.

$$\min_{\hat{I}\in\mathbb{R}^{\mathbb{N}_{\text{img}}}} \|\hat{I}\|_{l_1} \text{ such that } \|G\hat{I}-R\|_{l_2} \leq \varepsilon \tag{32}$$

where the parameter ε accounts for the noise and the model inaccuracies. This yields a BPDN beam forming algorithm, which is the basis of t-CBF.

V. RESULTS AND DISCUSSION

In this section, we present and discuss simulation results. We simulated a linear ultrasonic probe made of $N_{\text{el}} = 128$ elements. The central frequency is $f_c = 7.3$ MHz, which gives $\lambda = 211\ \mu$m at $c = 1540\,\text{m s}^{-1}$. The distance between the center of two consecutive elements is equal to λ in order to minimize the grating lobes. The sampling frequency is set to $f_s = 40$ MHz, which means that if the final image is a sector that spans 7 cm in azimuth and 7 cm in depth, each simulated Green's functions will be a 128×2000 sample matrix at least. After the column-wise *unwrapping*, this gives a 256 000 value vector. Now if we work on a grid $\mathcal{G}$ defined by the pitches $\Delta x = \lambda/2$ in azimuth and $\Delta z = \lambda/2$ in depth, we need to simulate roughly $670 \times 670 = 448\,900$ Green's functions. Using these parameters, the final matrix G will be a $256\,000 \times 448\,900$ matrix of double precision floating point numbers. Hence, the size of the entire matrix G would be roughly 920 GB. Having that matrix readily accessible in the random access memory (RAM) of the system is unrealistic. This first limitation could be mitigated by the use of a multicore graphics processor unit (GPU) card to compute the coefficients of G on-the-fly as opposed to storing them in the RAM. Another solution, that we chose to pursue in this article, is to restrain the simulation to a small domain of 192×192 pixels. Another important aspect is the computation time needed to calculate a single image. Here, MATLAB is used to carry out the computation for proof of concept. As a result, processing times can be significant. In the long run, a few strategies could be pursued to improve on this: the algorithm could be adapted to C language, heavy GPU parallelization could be used, etc. The following development focuses on off-line reconstruction.

All the pressure fields are simulated using Jensen's Field II.[22]

A. t-CBF using a plane wave excitation and 128 transducers in reception

In this section we simulate a homogeneous medium containing a finite number of point scatterers and we investigate the influence of the scatterers' position on the reconstruction.

1. One point scatterer simulation

For this simulation, a unique point scatterer is considered. The field-of-view (FOV) is a 192×192 pixel image and the pitch in azimuth and depth is $\Delta x = 5\lambda/2$ and $\Delta z = 3\lambda/2$, respectively. Attenuation is neglected as a first approximation, and the image is centered on $x = 0$ cm, $z = 2.5$ cm. The excitation is a plane wave: all the transducers fire the same pulse at the same time. The full aperture is used in reception. In Fig. 7, the point scatterer is located in the center of the image, at $x = 0$ cm, $z = 2.5$ cm. The results

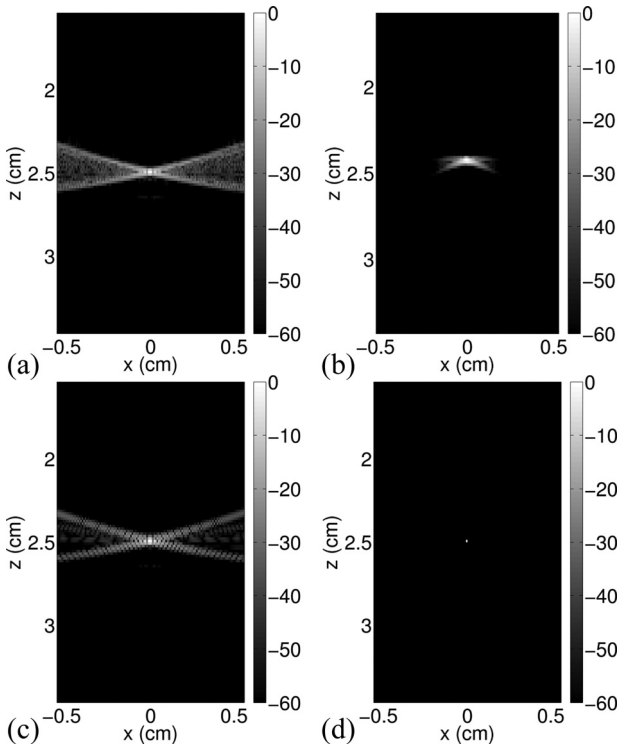

FIG. 7. Simulation of one point scatterer at azimuth 0 and depth 25 mm. Images obtained using: (a) plane wave DAS, (b) conventional DAS with 84 focalized transmit beams, (c) projection of the raw data on the matrix G, and (d) l_1-minimization.

from both the l_1-minimization and the dynamic focusing DAS (Ref. 12) are presented in Fig. 7.

The l_1-minimization recovers the map of the scatterers in the medium. The appearance of the image computed with DAS is different: it displays sidelobes and a coarser resolution. The differences between the methods may be explained by Eq. (26). The t-CBF would be a de-convolved version of the DAS image to a certain extent. For that reason, the result obtained through l_1-minimization is a single white pixel, whereas the image obtained using DAS shows sidelobes on each side of the point scatterer. Obtaining a comparable resolution with DAS would require many focalized transmit beams (typically 84, Fig. 7), or many plane wave excitations in the case of plane wave compounding (typically 12)[23] as well as a wide aperture.

2. Point scatterers selected at random

In this section we briefly look into the limits of the sparsity constraint. One of the main assumptions we have made so far is that the number of scatterers is relatively small. In that section, the ultrasonic field generated by 128 scatterers was simulated. The position and reflectivity of each scatterer are chosen at random on the grid $\mathcal{G}$. In Fig. 8, the images obtained using DAS, projections on the matrix G, and l_1-minimization are given for comparison. The reconstruction in Fig. 8(c) was very accurate, as the amplitude of each scatterer was recovered as well as their position. However, when the number of scatterers increases, the quality of the recovery decreases and the convergence time of the algorithm increases.

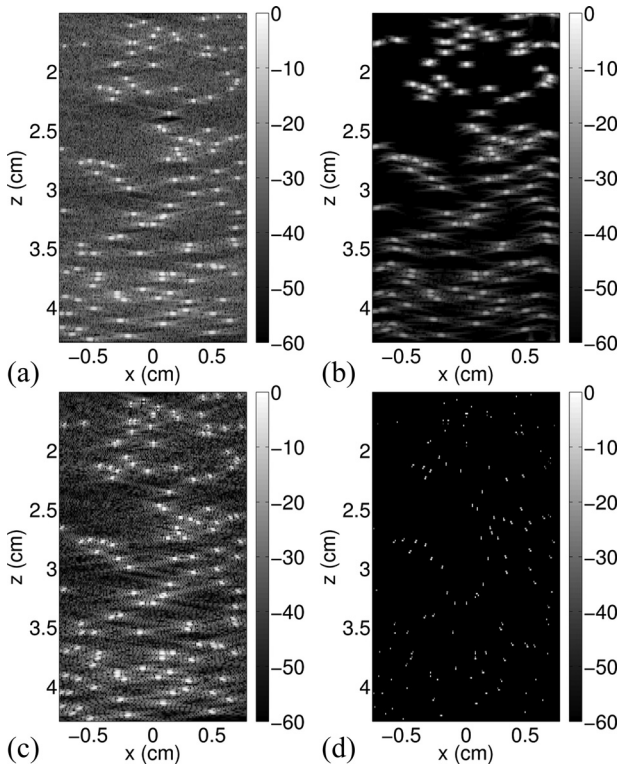

FIG. 8. Simulation of 128 point scatterers chosen at random on the grid $\mathcal{G}$. Images obtained using: (a) plane wave DAS, (b) conventional DAS with 84 focalized transmit beams, (c) projection of the raw data on the matrix G, and (d) l_1-minimization.

The resolution is much better than in the case of 84 transmit beams [Fig. 8(b)]. For that simulation, the point scatterers were located on a known grid, which made it easier for the algorithm to recover the map. However, the model was not perfect and the wavefronts generated for the simulation differed from the wavefronts stored in the dictionary G. The attenuation was not considered, and neither was the influence of the directivity of the transducers.

B. t-CBF using a plane wave excitation and 16 transducers in reception

One of the great benefits of CS is the ability to decrease the number of measurements necessary to perform an accurate reconstruction. In our case, that could mean acquiring less samples in time, or less samples in space, or both. It could also mean imaging a medium using less transmits. In this paper, we focus on acquiring less spatial samples, and less transmits, as it seems to be the most beneficial way to use CS for ultrasound beam forming.

The reduction of the number of transmits was implicitly used in the beginning of the paper: we assumed that the medium was insonified by a single plane wave. Usually, many focalized transmits are used to generate a single image, affecting the frame rate. The use of one, or a few, non-focalized transmits would allow for higher frame rates.

Reducing the number of transducers in acquisition can take several forms. In fact, using less elements in the probe raises a simple question: how to select the elements in a way that satisfies the principles of CS. The selection process is not trivial, as it directly impacts the mutual coherence of the measurement matrix. Figure 9 shows the evolution of the *mutual coherence* of the matrix G. It is generated by computing the scalar products of all the columns of G and sorting them by descending order of magnitude. The mutual coherence μ of a matrix G is commonly defined as the maximum absolute value of the cross-correlations of the columns of G,

$$\mu_G = \max_{1\le i,j\le N_{\text{img}}} |G_i^{\mathsf{T}} G_j|. \tag{33}$$

The acquisition using the entire aperture of 128 elements is here taken as a reference and compared against different element selection strategies: the signal is acquired using (a) the N_{acq} central transducers; or (b) N_{acq} transducers equally spaced, and spanning the entire aperture; or (c) N_{acq} transducers selected at random, and spanning the entire aperture, used throughout the acquisition; or finally (d) N_{acq} transducers selected at random at each time sample.

We simulate two scatterers: one is positioned on the grid $\mathcal{G}$ while the other one is off the grid. The reason for that experiment is that when the expansion of a wavefront originating from a point on $\mathcal{G}$ is evident, the expansion of the wavefront coming from a point off grid is not. It is expected to be wider.

1. On selecting the central transducers

A first strategy would be to select the central transducers of the probe, and to try to recover the image as if it had been acquired with the entire aperture. However, this approach leads to a high coherence of the measurement matrix and proves to be inefficient, as shown in Figs. 9 and 10(a). Using a smaller aperture means a loss in resolution as the main lobe of the PSF of the system becomes wider.[24] Therefore, if we consider a distribution of neighboring scatterers located in the vicinity of each other's main lobes it becomes evident that discriminating them would be a daunting task. The vectors of G corresponding to those points are highly coherent as the signals coming from them are very similar. Intuitively, we know that using a smaller aperture causes the

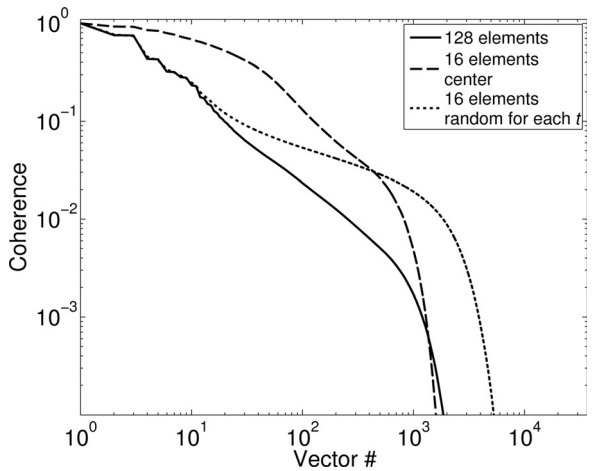

FIG. 9. Sorted coherence of sub-sampled G (dashed lines) vs complete G (continuous line): selecting only the central transducers leads to high coherence and a slow decay of μ, whereas selecting random transducers.

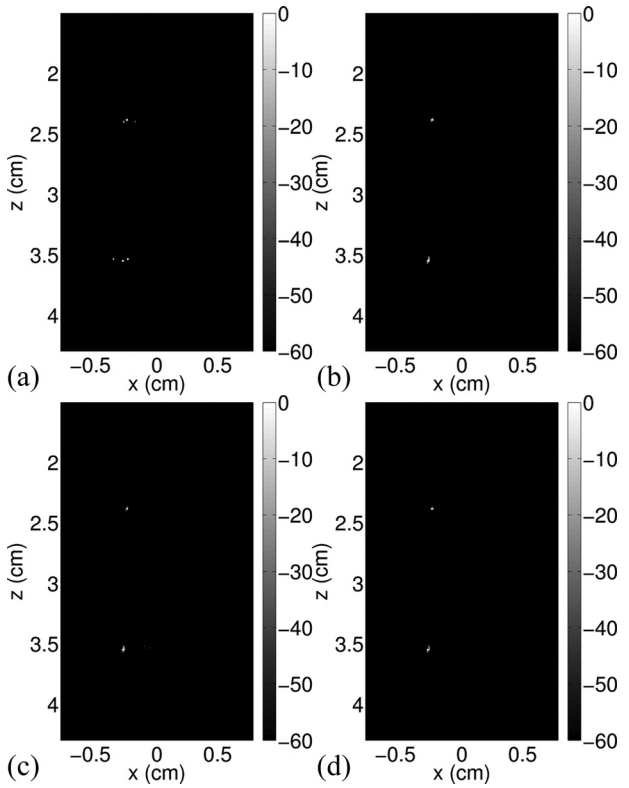

FIG. 10. Results obtained from sub-sampled data: (a) using 16 central transducers; (b) using 16 equally-spaced transducers spanning the entire aperture; (c) 16 randomly-spaced transducers spanning the entire aperture; and (d) using a different set of 16 randomly-chosen transducers for each time sample.

far-field of the probe to be shallower.[19] Hence, the deepest wavefronts acquired by the probe are very close to plane waves. The considered points being close to the axis of the probe, the waveforms generated by scatterers located within a few wavelengths from each other are highly correlated, making it harder for the algorithm to discriminate point scatterers in azimuth for a given depth. The result, shown in Fig. 10(a) is that the main lobe of the point on-grid is a few pixels wide, and the PSF of the off-grid point is wider and somewhat noisy. The algorithm was able to detect a scatterer at the right depth but it had more trouble discriminating it in azimuth.

2. On selecting equally spaced transducers spanning the whole aperture

To alleviate the limitation aforementioned, a second strategy would be selecting transducers across the entire aperture. It should be beneficial for discriminating scatterers in azimuth. This way, the algorithm is still using only a small subset of transducers, but the entire physical aperture is used. At first, we selected equally spaced transducers. In a classic setting and if the distance between transducers is greater than λ, the issue with using equally spaced transducers is the appearance of grating lobes.[24] In fact, the space between two transducers in an ultrasonic probe is calculated so that the angle at which the grating lobes exist is about 90° from the axis of the probe, minimizing their effect on image quality.

Surprisingly, the grating lobe artifact did not seem to affect the image quality too much, as can be observed in Fig. 10(b). The results are much better as the two PSFs are equivalent. The PSF of the point on-grid is almost a single pixel, as expected, whereas the PSF of the point off-grid is much narrower than in the previous case.

However, it is to be expected that due to the sidelobes, the coherence of G will be higher for points located in the secondary lobes of each other. As a result, an image with more scatterers would be less accurately reconstructed.

3. On selecting randomly spaced transducers spanning the whole aperture

In order to attenuate the grating lobe effect, another selection strategy would be to use a subset of randomly spaced transducers to make sure the grating lobe issue does not occur. Before acquisition, a subset of elements is chosen at random and used in the generation of the matrix G as well as in the acquisition process.

Figure 10(c) shows a result that is not fundamentally different from what was obtained previously, because the two scatterers are not located in the vicinity of each other's grating lobes.

4. On selecting randomly spaced transducers for each time sample

In order to decrease mutual coherence even further, one could think of using a different random set of transducers for each time sample. For example, if the user wants to acquire 1600 time samples with 16 transducers, a 16×1600 map of transducer numbers can be generated and used in the generation of G, as well as to perform the acquisition. This way, the acquisition basis is well-known and well-defined.

From Fig. 9, we can see that the performance improves in terms of coherence. For the neighboring scatterers, the coherence of the sub-sampled basis follows the one of the original one. In azimuth, the coherence decreases faster than what we observed in the previous cases.

The end result, shown in Fig. 10(d), displays an improvement in the focalization of the energy as the PSF is this time a single pixel exact for both the on-grid and off-grid points. The incoherence of G greatly improves the quality of the reconstruction.

C. t-CBF and super-resolution

1. Principle

In very specific conditions, we can hope to use CS to achieve super-resolution. In fact, the matrix G links a pixel to a wavefront like a dictionary. If the dictionary includes wavefronts originating from scatterers closer than $\lambda/2$, we can hope to separate them. Of course, one could object that with such a fine grid, the coherence of G will increase drastically. However, *in silico* experiments suggest that in the case of a model G that describes the data R exactly, super-resolution is indeed achievable. Similarly, the PSF of a point scatterer should be a single pixel without sidelobes. In that very specific case, the raw data R is generated using the

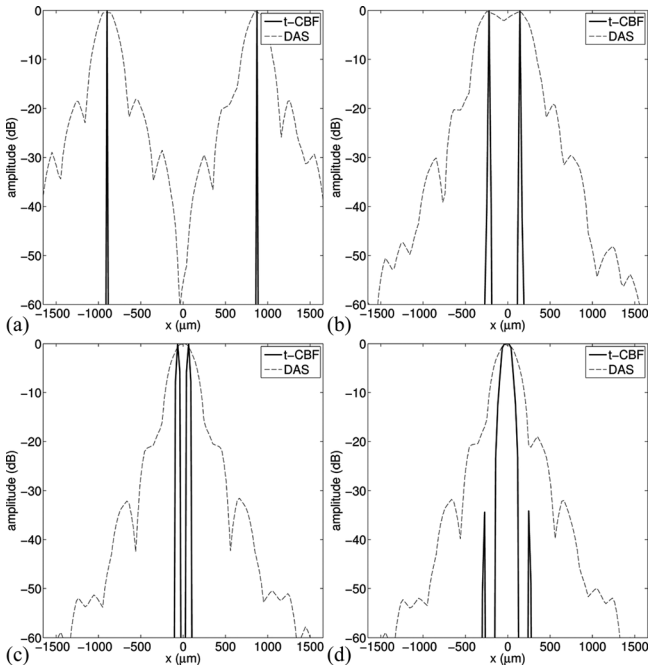

FIG. 11. DAS is used as a reference: (a) separated points: $\Delta x_s = 8\lambda$; (b) at the limit of separation for DAS according to the Rayleigh criterion: $\Delta x_s = 2\lambda$; (c) DAS no longer separates the two scatterers: $\Delta x_s = 2\lambda/3$; (d) t-CBF and DAS cannot separate the two scatterers: $\Delta x_s = \lambda/2$.

same function gauspuls mentioned in Eq. (29) than the matrix G. This way, we know that the raw data R corresponds to an image that is exactly sparse.

2. Results

For this experiment, a finer grid spacing of $\Delta x = \lambda/10$ in azimuth and $\Delta z = \lambda/10$ is used. The other parameters remain unchanged. We consider a homogeneous medium with two point scatterers located at the same depth but at different azimuths. The reconstruction algorithm is applied to the raw data generated analytically using Eq. (29). The DAS image is generated using a standard pulse sequence for a linear array such as the Philips L12-5: a translating aperture of 64 elements is used resulting in 64 focalized pulses fired *en face* the probe. The two scatterers are located at depth $z_s = 15$ mm. Figure 11 shows a performance comparison in terms of resolution between t-CBF and DAS. Four cases are presented: (a) the two scatterers are distant enough to be perfectly separated by DAS: the distance between the two scatterers is $\Delta x_s = 8\lambda$, (b) the scatterers are at the limit of separation as defined by the Rayleigh criterion: $\Delta x_s = 2\lambda$, (c) the scatterers are no longer separated by DAS but t-CBF can still separate the points, the classic reconstruction showing only one main lobe: $\Delta x_s = 2\lambda/3$, and (d) neither of the reconstructions can separate the scatterers: $\Delta x_s = \lambda/2$. Overall, the contrast seems better as it is not affected by sidelobes.

D. t-CBF on a wire phantom

1. Introduction

The last experiment is realized using an iU22 ultrasound scanner from Philips (Bothell, WA) with a modified

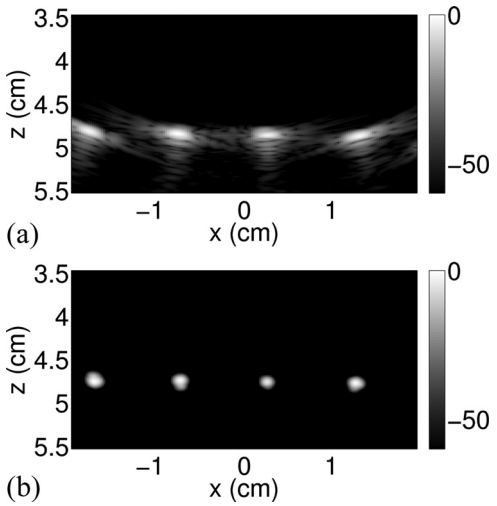

FIG. 12. Wire phantom.

hardware that allows us to acquire the raw data. The acquisition is done using a Philips S5-1 sector probe. The phantom is made of a series of taut fishing lines of diameter close to λ parallel to each other, in a water tank. The speed of sound in water is assumed to be unchanged throughout the experiment. S5-1 acquires echoes in a 2D plane perpendicular to the orientation of the fishing lines so that each of them acts as a point scatterer. This way, the expected image should be a set of aligned bright spots on a dark background, ensuring the sparsity we need for CS.

2. Results

Figure 12 shows the images obtained using DAS [Fig. 12(a)] and t-CBF [Fig. 12(b)]. For this particular experiment and because we are using a sector probe, the excitation wave is a diverging wave. The advantage of using a diverging wave is that if the parameters are chosen wisely the entire sector can be insonified at once. The image obtained with t-CBF appears more resolved, there are no sidelobes, and each wire is separated from the next and well-defined in space. The DAS image displays a lower resolution and intertwined sidelobes.

VI. CONCLUSION

Over the past decade, the importance of CS in the medical imaging world has increased drastically. So far, and to the best of our knowledge, that revolutionary inverse problem technique had never been applied for time-domain beam forming of ultrasonic fields. With this article, we presented a brief overview of CS, and more importantly we justified theoretically the feasibility and validity of the framework. Through simulations and experimentations we showed that an image of point scatterers can be recovered from the insonification of a medium by a single plane wave, when in the case of conventional DAS, more than a hundred focalized excitation pulses would be necessary and, in the case of plane wave compounding, more than ten excitation pulses would be required. We showed that the number of transducers in reception can be reduced from

128 to 16 transducers without significant loss of image quality. Finally, we showed that in specific, controlled conditions (near-perfect model, point scatterers on a known grid) t-CBF can be used to achieve super resolution of point scatterers.

The technique presented here is for time-domain beam forming. Other groups such as Schiffner and Schmitz[8] have proposed a CS framework in the frequency domain. However, the relationship between the two frameworks is direct. In fact, the matrix G used by Schiffner and Schmitz[8] is an under-sampled Fourier transform of the matrix G described in this paper.

As a result, the great potential of CS for ultrasonic beam forming has been formally proven. The next steps include, but are not limited to, working on decreasing the size of the matrix G while retaining all the information needed for the reconstruction, finding bases better suited to describing speckle and tissue structures, applying the algorithm to medical phantom, and eventually use the technique *in vivo*. Those aspects are currently being investigated. Some encouraging results have already been obtained and will be the subject of a future publication.

[1]E. J. Candès, "Compressive sampling," in *Proceedings of the International Congress of Mathematicians: Madrid* (August 22–30, 2006), invited lectures, pp. 1433–1452, European Mathematical Society Publishing House.

[2]R. G. Baraniuk, "Compressive sensing," IEEE Signal Process. Mag. **24**(4), 118–121 (2007).

[3]J. Romberg, "Imaging via compressive sampling [introduction to compressive sampling and recovery via convex programming]," IEEE Signal Process. Mag. **25**(2), 14–20 (2008).

[4]M. Lustig, D. Donoho, and J. M. Pauly, "Sparse MRI: The application of compressed sensing for rapid MR imaging," Magn. Reson. Med. **58**(6), 1182–1195 (2007).

[5]J.-Y. Lu, H. Zou, and J. F. Greenleaf, "Biomedical ultrasound beam forming," Ultrasound Med. Biol. **20**(5), 403–428 (1994).

[6]M. Tanter and M. Fink, "Ultrafast imaging in biomedical ultrasound," IEEE Trans. Ultrason., Ferroelectr., Freq. Control **61**(1), 102–119 (2014).

[7]J.-Y. Lu and J. Greenleaf, "Pulse-echo imaging using a nondiffracting beam transducer," Ultrasound Med. Biol. **17**(3), 265–281 (1991).

[8]M. F. Schiffner and G. Schmitz, "Fast pulse-echo ultrasound imaging employing compressive sensing," IEEE Int. Ultrason. Symp. **2011**, 688–691.

[9]D. Friboulet, H. Liebgott, and R. Prost, "Compressive sensing for raw rf signals reconstruction in ultrasound," IEEE Int. Ultrason. Symp. **2010**, 367–370.

[10]M. Mishali, Y. C. Eldar, and A. J. Elron, "Xampling: Signal acquisition and processing in union of subspaces," IEEE Trans. Signal Process. **59**(10), 4719–4734 (2011).

[11]S.-C. Wooh and Y. Shi, "Optimum beam steering of linear phased arrays," Wave Motion **29**(3), 245–265 (1999).

[12]K. E. Thomenius, "Evolution of ultrasound beamformers," IEEE Int. Ultrason. Symp. **2**, 1615–1622 (1996).

[13]E. J. Candès and M. B. Wakin, "An introduction to compressive sampling," IEEE Signal Process. Mag. **25**(2), 21–30 (2008).

[14]S. Chen and D. Donoho, "Basis pursuit," in *Conference Record of the Twenty-Eighth Asilomar Conference on Signals, Systems and Computers*, (1994) Vol. 1, pp. 41–44.

[15]E. J. Candès, J. Romberg, and T. Tao, "Robust uncertainty principles: Exact signal reconstruction from highly incomplete frequency information," IEEE Trans. Inf. Theory **52**(2), 489–509 (2006).

[16]M. A. Davenport, M. F. Duarte, Y. C. Eldar, and G. Kutyniok, "Introduction to compressed sensing," Preprint, Vol. 93, pp. 1–64 (2011).

[17]B. Angelsen, *Ultrasound Imaging: Waves, Signals, and Signal Processing*, Vol. 1 (Emantec AS, Trondheim, Norway, 2000), 680 pp.

[18]E. Van Den Berg and M. Friedlander, "Spgl1: A solver for large-scale sparse reconstruction," Online: http://www.cs.ubc.ca/labs/scl/spgl1 (Last viewed December 23, 2014).

[19]A. D. Pierce, *Acoustics: An Introduction to its Physical Principles and Applications* (McGraw-Hill, New York, 1981), pp. 153–207.

[20]S. X. Pan and A. Kak, "A computational study of reconstruction algorithms for diffraction tomography: Interpolation versus filtered-backpropagation," IEEE Trans. Acoust., Speech, Signal Process. **31**, 1262–1275 (1983).

[21]C. Dorme and M. Fink, "Focusing in transmit–receive mode through inhomogeneous media: The time reversal matched filter approach," J. Acoust. Soc. Am. **98**(2), 1155–1162 (1995).

[22]J. A. Jensen, "Simulation of advanced ultrasound systems using field ii," in *IEEE International Symposium on Biomedical Imaging: Nano to Macro*, (2004) pp. 636–639.

[23]G. Montaldo, M. Tanter, J. Bercoff, N. Benech, and M. Fink, "Coherent plane-wave compounding for very high frame rate ultrasonography and transient elastography," IEEE Trans. Ultrason., Ferroelectr., Freq. Control **56**, 489–506 (2009).

[24]J. Goodman, *Introduction to Fourier Optics* (McGraw-Hill, New York, 2008), pp. 32–62.